Isolating the detrapping of deuterium in heavy ion damaged tungsten via partial thermal desorption

M.J. Simmonds [a, *], T. Schwarz-Selinger [b], J.H. Yu [a], M.J. Baldwin [a], R.P. Doerner [a], G.R. Tynan [a, c]

[a] Center for Energy Research, UC San Diego, 9500 Gilman Dr., La Jolla, CA, 92093-0417, USA
[b] Max-Planck-Institut für Plasmaphysik, Boltzmannstrasse 2, D-85748, Garching, Germany
[c] Department of Mechanical and Aerospace Engineering (MAE), UC San Diego, 9500 Gilman Dr., La Jolla, CA, 92093-0411, USA

ABSTRACT

Partial Thermal Desorption Spectrometry (pTDS) progressively depopulated trapped deuterium (D) from heavy-ion damaged tungsten (W) to determine spatial location and detrapping energies. W samples were prepared identically: 5 MeV Cu^{2+} damaging ions (0.12 peak dpa dose) before D_2 plasma loading (10^{24} D/m^2 fluence) held at 373 K. Each sample reached one of six pTDS peak-and-hold temperatures. Nuclear Reaction Analysis (NRA) measured the D spatial profile remaining after pTDS, before final TDS.

NRA and TDS measured total D retention were in good agreement. NRA displayed three zones of D-populated defects: (I) near-surface (below 0.1 μm), (II) heavy-ion damage (peaked ~1 μm), and (III) uniform intrinsic (bulk). D concentration in zone I reduced by ~ 97% in samples with pTDS at 597 K and higher, indicating near-surface traps have low detrapping energy. The Stopping and Range of Ions in Matter (SRIM) predicts a displacement profile for zone II that coincided with measured D profile for samples with pTDS at 597 K and higher. Samples prepared with pTDS below 597 K display a distinctly different D profile in zone II. The complete cycle of D_2 plasma loading, pTDS, NRA, and final TDS was modeled with Tritium Migration Analysis Program (TMAP) using a recently developed Pseudo Trap and Temperature Partition (PTTP) scheme. Differences in TDS profiles isolated traps that release between consecutive pTDS temperatures, demonstrating 6 distinct release peaks. The best fit was found with detrapping energies near 1.0, 1.2, 1.4, 1.6, 1.8, and 1.9 eV. These results show that heating at 762 K for 2.5 h released ~99% of retained D in heavy-ion damaged W.

© 2019 Elsevier B.V. All rights reserved.

1. Introduction

The retention of tritium in Plasma Facing Materials (PFMs) is an important issue due to both safety concerns as well as maintaining the fuel cycle in fusion devices [1]. The production of fusion neutrons will lead to the degradation of PFMs throughout the bulk of the material. In order to study the effects of neutron damage and tritium exposure, heavy ion damage and deuterium are used as proxies, respectively. The guidelines for the use of heavy ions to simulate neutron damage are outlined in Ref. [2].

Experiments conducted to study displacement damaged W typically use NRA and TDS to quantify D retention. NRA probes the D distribution across the near-surface region up to depths of ~10 μm, whereas TDS measures the released D from throughout the bulk. NRA can not differentiate between trapped and solute D atoms located between W lattice sites, nor can it directly determine detrapping energy or trap type. Among other factors such as surface recombination, the release peaks for thermally desorbed D from W are correlated to both the spatial position and detrapping energy of a particular type of defect. The measured release rate from the surface is the result of the escape of D from multiple types of defects, each having a particular detrapping energy, followed by subsequent diffusion through the material to reach the surface where recombination occurs. The resulting TDS data may display one or more effective release peaks, due to nearby detrapping energies from multiple defects as well as multiple D fill levels for a single defect type.

Comparing the activation energies calculated with Density

Functional Theory (DFT) and attained by modeling thermal desorption data, various defect types in W have been associated with a particular dominant detrapping energy [3]. Inferred detrapping energies range for dislocations and grain boundaries from 0.8 to 1.0 eV, vacancies from 1.3 to 1.7 eV, and vacancy clusters from 1.8 to 2.4 eV. Detrapping energies may also overlap. Scanning transmission electron microscopy [4] suggests dislocation loops span 0.4—1.8 eV [5]. Though DFT predicts multiple D filling of some defects (e.g. mono-vacancies [6,7]) the individual release peaks may not be directly resolvable in TDS data if the detrapping energies are too close together. Note that the values determined from TDS data are dependent on both the attempt frequency, generally assumed to be 10^{13} s^{-1} [7], as well as the value used to model surface recombination.

Previous studies [3,8,9] have used varied sample temperatures during plasma exposure to selectively populate defects. At higher sample temperature, defects with lower detrapping energies can not be effectively filled with D if the release rate is large relative to the trapping rate. The increased temperature may significantly influence the evolution of defects to be populated, complicating the interpretation of such experiments. For instance, mono-vacancies may be partially annealed as they recombine with mobile interstitials, and between 523 and 573 K the vacancies become mobile and can further annihilate or agglomerate into clusters [10,11]. Positron annihilation spectroscopy shows that the clusters grow in samples heated to 650 K in under 5 min [12]. Thus, at high sample temperatures, the assumption of a static population of defects during plasma exposure may no longer be valid. In addition, the increased diffusivity of D at higher temperature may increase retention as deeper intrinsic traps become filled. This results in the broadening of each release peak. Therefore the direct comparison of samples prepared with various sample temperatures during plasma exposure is not straightforward.

To better quantify the spatial location and detrapping energies associated with various defects, we devised an experimental approach to sequentially depopulate each defect according to detrapping energy. Whereas previous experimental studies that attempted to model NRA and TDS data have assumed specific detrapping energies and spatial concentrations, this approach aims to constrain both quantities and test if a discrete detrapping energy model can reproduce the experimental data. Similar to the approach by Efimov et al. [13], all damaged and D decorated samples have the same initial conditions prior to pTDS. Unlike Efimov, by holding the sample at a fixed elevated temperature (peak-and-hold) after the pTDS linear ramp, defects with appreciable release rates at that temperature will further depopulate. The released D then either travels further into the material, filling traps with higher detrapping energy, or reaches the surface to escape the sample. NRA is carried out after each pTDS procedure to provide a spatial profile of the remaining D atom concentration. The resulting data allows us to then infer the spatial profile with respect to detrapping energies and densities from each spatial zone attributed to plasma-induced, heavy ion beam induced, and intrinsic trap sites.

Typically the TDS temperature ramp is assumed fast enough to neglect defect evolution, while the pTDS peak-and-hold may change the defect population. Since pTDS temperatures in this experiment span 467—762 K, mono-vacancies may become mobile but vacancy clusters would not dissociate (~1200 K [14]). Additionally, traps may agglomerate migrating defects that can result in an increase to the detrapping energy.

In a similar experiment, Zhao et al. [15] performed pTDS on W samples with 0.01 and 1 displacements per atom (dpa). The resulting full TDS profiles show that the initial release for the 0.01 dpa sample starts at a temperature well above the peak-and-hold

and slightly above initial release for the 1 dpa sample. Here it is worth noting that the full TDS of the 0.01 dpa sample does not exhibit obvious defect evolution due to the pTDS. On the other hand, the 1 dpa does show that the highest temperature release peak significantly grew, likely due to vacancy agglomeration during the peak-and-hold.

In some previous experiments, within the heavy ion damage region there is a discrepancy between some experimental NRA data and SRIM predicted damage profiles. NRA data from plasma exposure at elevated sample temperatures (~600 K and above) [8,9,12,16] do not display a significant near-surface peak and are spatially commensurate with the SRIM calculated dpa profile. Yet lower sample temperature during plasma exposure yields a D concentration in the near-surface that can not be explained by plasma induced defects alone. The deviation in trap profile and consequently D concentration measurements is likely due to a different spatial profile for low detrapping energy defects.

2. Experiment

2.1. Sample preparation

W samples originated from a certified 99.95 wt% powder metallurgy polycrystalline rod, 6 mm in diameter and cut into disks 1.5 mm thick. The plasma facing surface received a mirror-like finish by successive polish treatments ending with a 3 μm grit. Arithmetic mean surface roughness, measured with a confocal microscope, resulted in 28 ± 5 nm after polish. Contaminants from polishing were removed in successive ultrasonic baths of acetone followed by ethanol. Next, the samples were annealed at 1173 K for 1 h in a vacuum chamber below 10^{-4} Pa. As noted in Ref. [17], a broken W sample displayed elongated grains perpendicular to the surface with dimension on the order of 10 μm parallel to the surface, as viewed by a scanning electron microscope. The maximum annealing temperature is well below the recrystallization temperature, leaving an intrinsic level of various defects throughout the bulk of the sample.

2.2. Heavy ion damage

The previously prepared W samples were irradiated with 5.0 MeV Cu^{2+} ions at the TOF beamline of the tandem accelerator laboratory at Max-Planck-Institut für Plasmaphysik in Garching (IPP) while under a low vacuum of 10^{-6} Pa and held at 295 K with a water-cooled sample holder. Details of the setup can be found in Ref. [18]. The beam had a full width at half maximum of 2 mm, and was rastered over the samples to achieve lateral homogeneity. The implanted Cu dose was 1.215×10^{18} ions/m^2 with an average flux of 2.4×10^{15} ions/m^2/s, which maintained an impurity level below the intrinsic Cu level [19]. In accordance with Stoller et al. [20], the "Quick" Kinchin-Pease option and a displacement damage threshold of 90 eV were used to calculate the displacement profile in SRIM shown in Fig. 1 with a peak dpa of 0.12. According to the simulation, on average each energetic Cu ion is estimated to produce a collision cascade with over 5600 W lattice displacements. This sample temperature during plasma exposure was low enough to avoid the annealing of displacement damage that we have reported in previous work [17].

2.3. D_2 plasma exposure

One undamaged sample, as well as the identically prepared Cu ion irradiated samples, were exposed to D_2 plasma with a neutral pressure of 0.7 Pa in the PISCES-E device, a plasma etcher with a 13.56 MHz RF source [21]. The air-cooled sample holder was
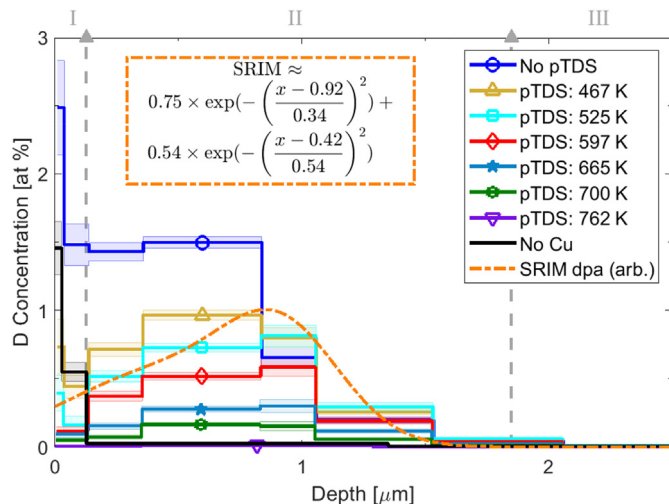
Fig. 1. The D concentration measured through NRA decreases with increasing pTDS temperature. The SRIM predicted trap profile (dot-dashed orange) for 5 MeV Cu^{2+} displays a peak near $\sim 0.9\,\mu m$ and shown here scaled to 1. Note that the experimental dose resulted in a calculated peak dpa of 0.12. A two Gaussian fit to the SRIM profile is defined by the normalized function. Dashed silver vertical lines indicate the approximate transition between zones I-III. (For interpretation of the references to color in this figure legend, the reader is referred to the Web version of this article.)

The equation shown in the figure:
$$SRIM \approx 0.75 \times \exp\left(-\left(\frac{x - 0.92}{0.34}\right)^2\right) + 0.54 \times \exp\left(-\left(\frac{x - 0.42}{0.54}\right)^2\right)$$

negatively biased to implant D with an ion impact energy of 110 eV and maintained the sample at 373 K as measured by a thermocouple in contact with the rear of the sample. An RF compensated Langmuir probe inferred an average flux ($\Gamma_{incident}$) of 1.8×10^{20} ions/m^2/s uniformly across the surface of the sample holder as detailed in Ref. [22]. Each sample received a total fluence of 10^{24} D/m^2 after ~ 1.5 h.

2.4. Partial TDS

The plasma-exposed samples were kept at room temperature for 25 days before being subjected to pTDS. Samples were mounted on the tip of a thermocouple within a vacuum below 10^{-6} Pa. Parabolic mirrors focused the heat from infrared lamps on the sample surface. A programmable controller was set to heat the samples at a constant rate of 0.5 K/s before plateauing for 2.5 h at a particular peak-and-hold temperature. That is, instead of completely desorbing the sample as in a typical TDS run by heating the samples to a peak temperature near 1300 K, temperatures well below that were chosen to selectively depopulate the corresponding lower energy traps. In what follows, the label for each pTDS sample refers to this peak-and-hold temperature (e.g. "pTDS at 467 K"). It should be noted that two control samples were not thermally desorbed at this stage, one without pTDS labeled "No pTDS" and one without heavy ion damage, "No Cu".

2.5. NRA

NRA was performed on each sample at IPP Garching 20 days after the pTDS procedure. The D ($_3$HE,p)4He nuclear reaction measured the depth profiles of the remaining D concentration as prescribed by Mayer with a detector positioned at a scattering angle of 135° [23]. A $_3$HE ion beam was used to probe the first $\sim 6\,\mu m$ of D implanted in W with decreasing energies of 3.5, 2.5, 2.0, 1.65, 1.5, 1.3, 1.1, 0.8, and 0.6 MeV. Both the energy spectra of the resultant protons and alphas were captured in solid state detectors to determine the depth distribution of the retained D. Relative to the protons, the resulting alpha particles are only detectable for low

$_3$HE beam energies since the energy of reflected 3He ions overlap with the alpha energy. Probing with a $_3$HE energy slightly below and above the cross section peak (i.e. 0.6 and 0.8 MeV) enhances the near-surface resolution of D concentration. In addition to detecting both product ions, the various sources of straggle are minimized with relatively low probing energies. As a result, we can resolve D trapped within the near-surface (~ 100 nm) region; deeper NRA results have poorer spatial resolution. Using the NRA data, both SimNRA and NRADC were then employed to determine the most probable D concentration as a function of depth [23,24].

2.6. Final TDS

A further 18 days elapsed between NRA and the final TDS run where all samples were heated with a constant 0.5 K/s ramp rate up to a peak temperature above 1300 K to ensure full desorption of D. The partial pressures of H_2, HD, and D_2 were measured with a quadrupole mass spectrometer (QMS). The thermally desorbed particle flux was calculated by converting the QMS measured partial pressure via a calibrated D_2 leak. The total D flux was calculated as described in further detail by Yu [25], as the sum of the HD and twice the D_2 flux. Note that the HD flux was calibrated to the D_2 leak, without any further correction for ionization efficiency. Since the detection efficiency is expected to increase for ions of lighter mass this procedure leads to a small overestimation of the total D flux. However, as HD contributed only an average of 28% to the total D flux this is of minor importance. As described previously [17], variable ambient laboratory humidity, temperature, and length of vacuum break influence the water content adsorbed to the TDS chamber walls. This leads to a significant H_2 background signal that was scaled to and subtracted from the raw HD and D_2 signals.

3. Results

After the pTDS procedure was applied to each sample, and prior to final TDS, the spatial profile of D concentration in each sample was measured with NRA. In Fig. 1, the experimental data displays a monotonic decrease in D concentration as the pTDS peak-and-hold temperature is increased. The estimated error determined by NRADC as a concentration range is indicated as the corresponding transparent colored region in the figure. The NRA profiles have distinct spatial zones, labeled I-III respectively: zone I composed of the near-surface ($\sim 0.1\,\mu m$) region, zone II composed of the Cu damage ($\sim 1\,\mu m$) region, and zone III composed of the bulk of the samples depth. Within zone I, the control sample without heavy ion beam damage (solid black) displays a peak D concentration near 1.5 at. % that decays exponentially with a characteristic length of $0.05\,\mu m$. The intrinsic defects left after sample preparation annealing (below the recrystallization temperature) are assumed to have a uniform distribution throughout the bulk, zone III. For Cu ion beam damaged samples, the dominant contribution to total D retention is seen in zone II. The D concentrations for pTDS temperatures of 525 K and higher largely coincide with the SRIM predicted damage profile (dot-dashed orange). The "No pTDS" and the 467 K pTDS samples have profiles that are more heavily weighted closer to the surface. The small, but measurable, D level near $2\,\mu m$ suggests the D diffusion front reached beyond the SRIM profile, which was confirmed by subsequent TMAP modeling that predicted the front reached $\sim 20\,\mu m$.

In Fig. 2, the surface flux of D atoms released from the W samples during each pTDS and final TDS are shown as dashed and solid lines respectively. The 700 K pTDS sample is not shown due to an experimental error with the initial temperature ramp. The pTDS profiles (dashed lines) display the sequential removal of D from traps with increasing pTDS temperature, and exhibit a sharp drop
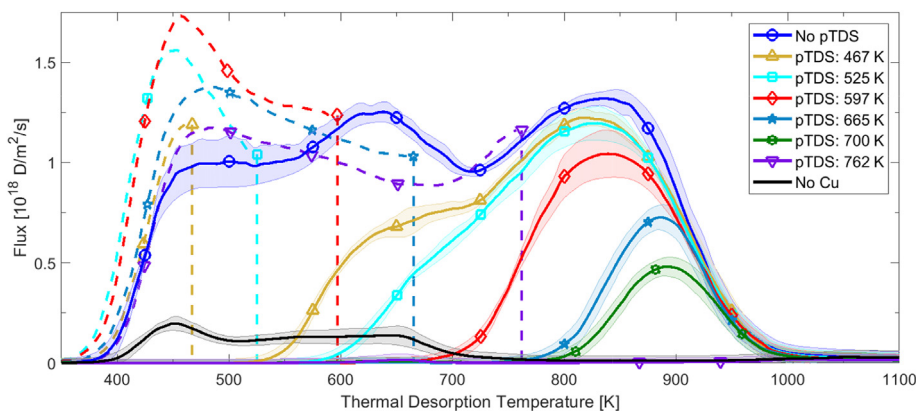
Fig. 2. The D surface flux during pTDS (dashed) and the final TDS (solid) are plotted with respect to a 0.5 K/s linear heating ramp. Once pTDS samples reached a specific peak-and-hold temperature, the flux during the 2.5 h peak-and-hold decays exponentially in time and approaches zero at this fixed temperature.

in released D flux when fixed at their peak-and-hold temperature. This D flux plotted against time instead of temperature displays an exponential decay during the pTDS peak-and-hold (not shown here but similar to Ref. [15]), indicating the depopulation of traps that exhibit a significant release probability at the pTDS peak-and-hold temperature. The first and weakest D filled traps are highly sensitive to surface conditions and storage time in between D implantation and TDS [26,27]. Whereas the pTDS samples were thermally desorbed after ~1 month, the control samples waited ~2 months. That extra storage time likely led to the "No pTDS" control (dark blue) having a lower first peak than in the other Cu damaged samples. The "No pTDS" control sample shows a significant increase in the amount of released D as compared to the "No Cu" control sample (black) for all temperatures below 1000 K. The initial release of the "No pTDS" control sample begins near the 373 K plasma exposure sample temperature. For all cases, it appears that the pTDS peak-and-hold temperature is at least 40 K lower than the leading edge of the initial release temperature during the subsequent final TDS. For example, the sample with a pTDS peak-and-hold temperature of 467 K (dashed gold) only begins to appreciably release D when the temperature exceeds 510 K during the subsequent final TDS (solid gold). This separation indicates that the underlying assumptions of the PTTP scheme [28] can be used to distinguish and isolate traps with progressively higher release energies. As a result, taken together the NRA and TDS data can be used to quantify the location and concentration of D residing in each trap, as illustrated in the following discussion.

Note that in Fig. 1, the NRA profiles for the control samples labeled "No Cu" and "No pTDS" have a high D concentration located in zone I. In the "No Cu" case this zone I population forms the majority of retained D inventory, while for the "No pTDS" case (which did suffer Cu ion beam damage) the zone I retained population sits on top of a significant retained D inventory located deeper in zone II. Comparing the "No pTDS" and the 467 K and 525 K pTDS cases in Fig. 1, we observe that the zone I retained D inventory is largely reduced, and is undetectable for the 597 K pTDS case shown in red in Fig. 1. Furthermore, the "No Cu" (solid black) and 597 K (solid red) final TDS curves in Fig. 2 display a crossing near 700 K. These observations show that the majority of the "No Cu" sample D inventory that was trapped in zone I has been completely released at 700 K whereas the ion beam damaged sample that underwent a 597 K pTDS treatment is just beginning to release D at this temperature. Considering Figs. 1 and 2 results together, we can then conclude that the zone I traps are induced by the plasma and have relatively low detrapping energies that release at temperatures below 700 K. Furthermore, we can conclude that

most of the increased inventory in ion beam damaged samples is located in zone II and releases at higher temperatures. These two experimental observations suggest that the NRA, pTDS, and final TDS approach used here may permit the inference of both spatial distribution of traps with differing trapping energies. We take up a deeper examination of the utility of the combined NRA, pTDS, and final TDS data sets after examining the self-consistency of the overall retention data emerging from these combined techniques.

By integrating the NRA profile over the depth into the material we can determine the remaining retained D inventory for each pTDS case. The result of this analysis is shown by the black circle symbols in Fig. 3, and shows a gradual reduction in the retained D as the pTDS peak-and-hold temperature is increased. Likewise, by integrating the pTDS release histories shown by the dashed curves in Fig. 2, we can determine how much D was released for each pTDS case. The result of this analysis is shown by the filled blue upright triangle data points in Fig. 3, and shows a gradual increase in the amount of released D with increasing pTDS peak-and-hold temperature. Finally, integrating the final TDS release curves shown by the solid curves in Fig. 2, we can determine the remaining D
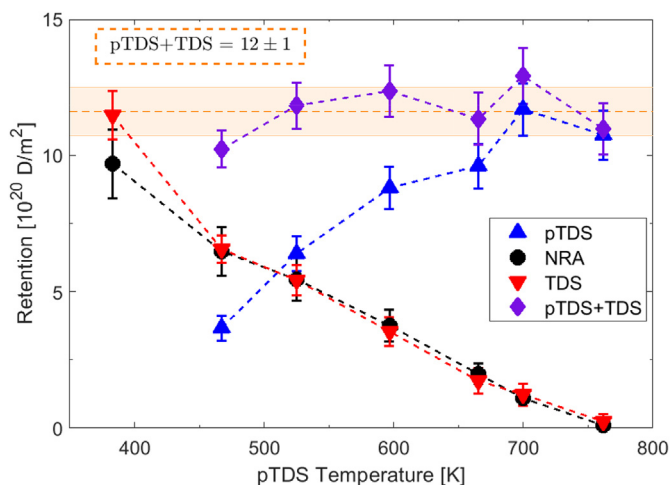

Fig. 3. The sum total D retention measured in the first 5.5 μm through NRA and the bulk through TDS. Plotted at the plasma exposure sample temperature of 373 K, the "No pTDS" sample shows the largest deviation from NRA. The sum of D retention measured from pTDS and TDS is consistent as seen by the average (orange shaded region). Dashed lines are only shown to guide the eye. (For interpretation of the references to color in this figure legend, the reader is referred to the Web version of this article.)

inventory throughout the bulk of the material. The result, shown as the inverted red triangles in Fig. 3 shows a gradual decrease in retained D inventory as the pTDS peak-and-hold temperature is increased, and is in good quantitative agreement with the NRA results. The sum of the pTDS and TDS data (purple diamonds) provides an independent measurement of retained inventory and shows a nearly constant value of $(12\pm1) \times 10^{20}$ D/m^2, consistent with the data point obtained from the damaged control sample ("No pTDS" in Figs. 1 and 2) which is plotted at 373 K on the x-axis in Fig. 3. Thus the independent NRA, pTDS, and final TDS techniques give consistent retained inventory measurements.

4. Isolating detrapping energies

The simulation of the pTDS, NRA, and final TDS stages are well constrained by both the identical initial conditions and the controlled depopulation of each trap. Here we assume each trap concentration and spatial profile as well as the filling thereof during D implantation are the same for all samples prior to the application of the pTDS procedure. In what follows, we exploit the selective depopulation of traps with lower detrapping energies in order to isolate the spatial location and detrapping energy of the desorbed D. In order to do this, for a given NRA profile or pTDS release dataset, we subtract the next highest pTDS temperature dataset (i.e. consecutive pTDS temperatures). The difference then can be used to determine spatial location (from differential NRA data) or release temperatures (from differential final TDS data). Furthermore, the spatial location of a given trap energy will be described by a spatial profile function ($f_k^j(x)$) that corresponds to the spatial distribution of the D that was released during consecutive pTDS exposures; we will find that this function will be zone (j) and trap type (k) dependent.

4.1. NRA subtraction

The NRA D profiles shown in Fig. 1 display a distinctly different shape for pTDS samples subjected to peak-and-hold temperatures of 525 K and above. Fig. 2 shows the remaining D in these higher temperature pTDS samples are trapped in defects with increasing detrapping energy. Fig. 4 displays the concentration difference profiles (ΔC) computed as the difference between consecutive NRA

D profiles and labeled by the two pTDS temperatures used to produce a given profile. The difference profiles for these higher temperature pTDS samples and the 762 K pTDS sample display a peak at a depth of 0.7–1.0 μm, in agreement with the SRIM predicted dpa profile (dot-dashed orange), showing that the computed dpa distribution at a given depth is correlated to the difference concentration at that location. We therefore use the SRIM predicted spatial profile to define the spatial profile function $f_{high}^{II}(x)$ for zone II, where the trap type ($k = high$) refers to high detrapping energies associated with higher temperature release.

In Fig. 5, the D concentration profile for the "No Cu" sample (black) displays a large near-surface component in zone I due to D_2 plasma exposure (note the much larger concentration scale compared to Fig. 4). The profile exponentially decays into the bulk as seen in previous work [29,30]. A fit (dot-dashed red) to the "No Cu" is shown as an intrinsic concentration plus an exponential decay with characteristic length of 0.05 μm. The exponential fit to the plasma induced trap distribution in zone I is then chosen to define the spatial distribution $f_{low}^I(x)$, where "low" refers to low detrapping energy traps (i.e. Fig. 4 shows $f_{high}^I(x)$ equals zero).

In order to isolate and determine the spatial location of low energy traps in zone II, both the "No Cu" and 597 K pTDS profiles are subtracted from the "No pTDS" profile (solid blue). First, noting the similarity in D profile for zone I between the "No Cu" and "No pTDS" NRA data shown in Fig. 1, we assume the plasma induced traps are represented by the "No Cu" profile. Second, the samples with pTDS peak-and-hold temperature at 597 K and above display no additional zone I component. Lastly, as shown in Fig. 4, these higher temperature pTDS samples display a D concentration coincident with heavy ion induced traps located in zone II. Thus the remaining D found after subtracting both the "No Cu" and 525 K pTDS reveals the profile for heavy ion induced traps associated with lower detrapping energies. An empirical fit to this difference ($f_{low}^{II}(x)$) is shown in Fig. 5 as the sum of two Gaussians (dot-dashed magenta), though the two distinct features may simply be an artifact of the NRA resolution. This difference-concentration distribution is quite distinct from both the near-surface zone I concentration profile, and the trapped D located within higher detrapping energy traps found in Fig. 4.
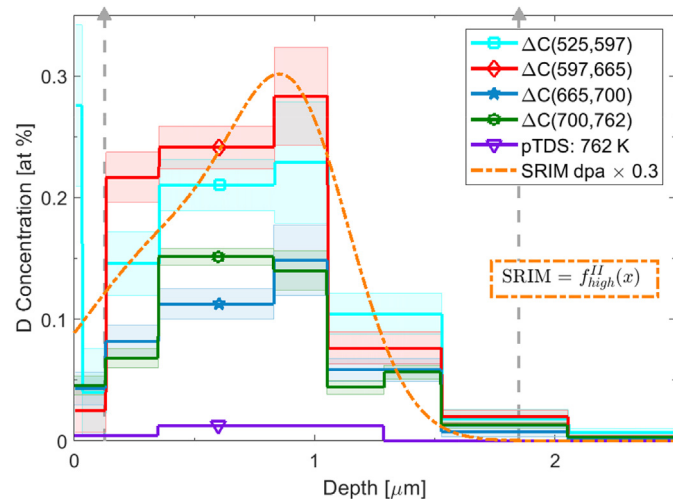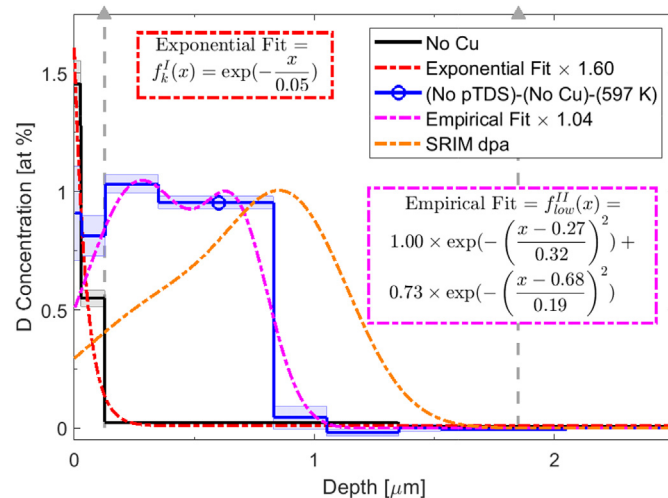

Fig. 4. The difference in D concentration between consecutive pTDS samples are shown as solid lines. The damage profile of zone II is further defined and fit well by the SRIM dpa profile scaled to 0.3 for ease of comparison (dot-dashed orange). (For interpretation of the references to color in this figure legend, the reader is referred to the Web version of this article.)

Fig. 5. The 'No Cu" sample is shown as solid black with an exponential decay function (dot-dashed red). The solid blue line representing "No pTDS," subtracting both the "No Cu" and 597 K pTDS NRA profiles, isolates the low energy traps due to heavy ion damage. An empirical fit (dot-dashed magenta) to this D profile is significantly shallower than the SRIM profile (dot-dashed orange). (For interpretation of the references to color in this figure legend, the reader is referred to the Web version of this article.)

4.2. TDS subtraction

Similarly, the differences between the final TDS data obtained from consecutive pTDS peak-and-hold temperature runs are shown in Fig. 6. Using the difference-flux ($\Delta\Gamma$) TDS profiles, we can infer the minimum number of distinct traps in damaged W. The first difference (dark blue) is too broad to be due to a single trap but would appear to have at least two detrapping energies. The separation and width of each additional difference suggest at least four more individual detrapping energies. Note that the overlapping initial release of the last two differences (turquoise and green) is likely due to the same detrapping energy. Lastly, the highest pTDS temperature at 762 K (purple) may have a unique detrapping energy of its own as further evidenced by the corresponding NRA profile in Fig. 4. Thus, there are likely at least 6 or 7 unique detrapping energies needed to model this data set obtained with a sample temperature of 373 K during plasma exposure, as seen in previous work [13,28,31].

These difference datasets obtained from NRA and final TDS measurements can be used to constrain a reaction-diffusion model of the D in damaged W to determine the spatial distribution and trapping energy that best reproduces these observations. We take up this modeling effort in the following.

4.3. TMAP simulation with PTTP

In order to use the verified and validated reaction-diffusion code TMAP7 [32–34] to model these results that require more than three types of traps with distinct detrapping energies, we employed a Pseudo Trap and Temperature Partitioning (PTTP) scheme as outlined and applied to TMAP7 [28]. In brief, for a particular temperature range this scheme utilizes a pseudo trap that accounts for multiple traps with deep energy wells that do not appreciably release but may act to trap mobile D from solute. When applied to TMAP7, only three traps are modeled at a time: the two lowest detrapping energy traps are included and can act to both trap and detrap D atoms, and a pseudo trap (which models all traps with higher detrapping energies) is included and primarily acts to trap D atoms.

Reaction-diffusion parameters as outlined in Refs. [26,28] were used and detailed in Table 1. During the D_2 plasma exposure phase, the implanted D flux was simulated as a Gaussian with mean depth ($r_{implant}$) and standard deviation ($\sigma_{implant}$) with a reflection coefficient (R).

The heavy ion damage, together with the intrinsic defects

Table 1
Summary of fixed parameters and activation energies (E_a) used in the TMAP simulation.

Ref.	Parameter			E_a [eV]
[6]	D_s	1.6×10^{-7}	[m^2/s]	0.25
[35]	K_r	$3 \times 10^{-25}\, T^{-1/2}$	[m^4/s]	−2.06
[7]	ν_0	10^{13}	[1/s]	
[36]	R	0.65		
[36]	$r_{implant}$	4	[nm]	
	$\sigma_{implant}$	2	[nm]	

leftover after sample preparation and annealing act as the initial trap concentrations for zone II and III respectively. Since TMAP7 uses a static trap concentration, here we also take the plasma induced trap profile in zone I as an initial condition. The formation of plasma induced defects is postulated to be due to a solute D saturated region stressing the near-surface zone I [29]. As detailed in Ref. [37], equation 1 estimates the diffusion limited D solute maximum concentration during D implantation. Using the parameters from Table 1 and sample temperature (T) during plasma exposure gives a D saturation level that approaches 2×10^{-4} at. %. TMAP simulations show that within 1% of total exposure time (< 1 min), the solute concentration has reached this saturation value. Compared to the total plasma exposure time of over an hour, the time required for plasma to induce these traps through saturation of zone I is relatively short and simply approximated as an initial trap concentration.

$$C_{s,max} \approx \frac{(1-R) \cdot \Gamma_{incident} \cdot r_{implant}}{n_W \cdot D_s(T)} \qquad (1)$$

Equation (2) defines the total initial trap concentration ($C^o(x)$) as a summation over trap type and spatial zone. Each trap type (k) is identified by a distinct detrapping energy (E_k). Note that the traps are ordered according to increasing detrapping energy. Each spatial zone (j = I, II, or III) has an associated profile function ($f_k^j(x)$), that is chosen according to the inferred trap distributions found from experimental data and shown in Figs. 4 and 5. All the profile functions are normalized to a peak value of unity. The profile function is multiplied by the peak concentration (C_k^j) for each trap and zone. For j = I, the exponential fit detailed in Fig. 5 defines the profile function. For j = III, the profile function is simply a constant. We also differentiate the particular trap profile in zone II for low and high energy traps as seen in Figs. 4 and 5. For j = II, the lower
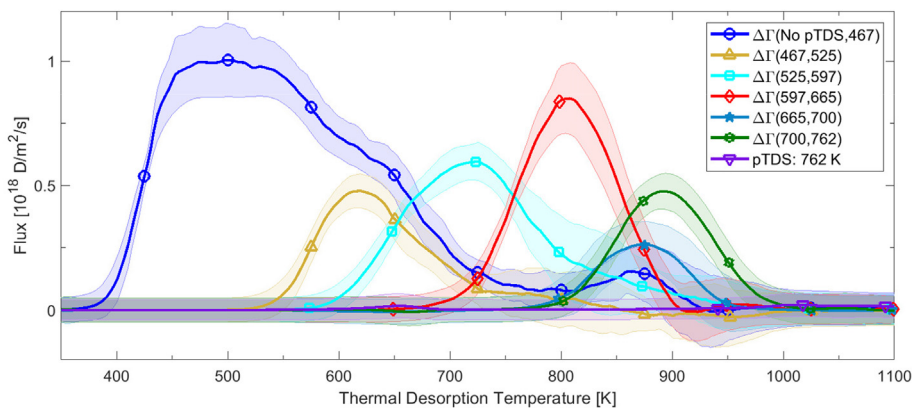

Fig. 6. The difference in D flux during final TDS ($\Delta\Gamma$) for each consecutive pTDS sample pair are shown. The first dark blue line displays a broader primary peak than the other differences. Each of the remaining differences can be modeled with a single detrapping energy. All of the differences, except for the green line, begin to escape the sample at a unique temperature. (For interpretation of the references to color in this figure legend, the reader is referred to the Web version of this article.)

detrapping energies use the empirical fit shown in Fig. 5 for zone II, while the higher detrapping energies use the SRIM profile. As a result of constraining the profile functions by experiment, the peak concentration (C_k^j) for each trap (k) in each zone (j) and the detrapping energies (E_k) become the free parameters that can be adjusted within TMAP7 in order to fit the experimental NRA and TDS data. Note that the sample preparation and D implantation phase are assumed identical for all samples in this dataset, thus we need only model this part of the experiment once for a given set of free parameters.

$$C^o(x) = \sum_k C_k^o(x)$$
$$= \sum_k \left[C_k^I f_k^I(x) + C_k^{II} f_k^{II}(x) + C_k^{III} f_k^{III}(x) \right] \quad (2)$$

4.4. Annealing defects

While the assumption of a static trap concentration is likely valid for a relatively fast temperature ramp (e.g. 0.5 K/s), the peak-and-hold during pTDS may allow for significant trap evolution. Sakurada et al. [38] presents D retention data from post damage (6 MeV Fe, 0.1 dpa) annealed W. Noting the similarity of damaging species, energy, and dpa level as well as the clear TDS release peaks, we inferred the reduced trap fraction (δ_k) with respect to each TDS release peak. Table 2 summarizes the reduction values at several anneal temperatures (T_{anneal}) and a linear interpolation determined the reduction value at each pTDS temperature. In this simplified model, traps are removed (e.g. Frenkel pair recombination), while defect agglomeration is neglected. Once again, since TMAP7 uses a static trap concentration, the removal of defects may be modeled incrementally. The first 30 min of the peak-and-hold duration was broken into 100 equal time increments and at the end of each increment a hundredth of the estimated reduced fraction ($0.01\delta_k$) was removed from the trap population. D was conserved as filled traps were removed by moving the excess D to solute concentration. Including trap removal provides the best agreement with experimental data and are the parameters presented in Table 2.

4.5. Fitting results

The complete cycle of D_2 plasma exposure, pTDS, and final TDS was simulated for each sample and all free parameters were optimized utilizing the technique of simulated annealing [39]. During the simulated annealing, the free parameters were constrained according to the differences in consecutive TDS and NRA data previously outlined. The simulation of a particular set of trap parameters results in unique NRA and TDS profiles. Both the experimental and simulation data were interpolated to a finely spaced

grid to directly compare the "goodness of fit." The Normalized Root Mean Square Error (NRMSE) as well as the Normalized Mean Absolute Error (NMAE), defined by the absolute difference between experiment and simulation, were the metrics used to determine the optimal fit. In addition, the resulting NRMSE and NMAE were weighted with respect to their total D retention and added together to determine a single fit metric. For instance, the "No pTDS" sample had the highest D retention and had the largest weight while the highest temperature pTDS at 762 K contributed the least weight when determining the best fit parameters.

The number of traps used to simulate the experiment was varied from 5 to 9. As outlined in the section on TDS subtraction, the best fit was found with 6 traps with detrapping energies near 1.0, 1.2, 1.4, 1.6, 1.8, and 1.9 eV. Using 7 traps, nearly the same energies were found and one additional energy of 2.4 eV produced nearly the same fit metric. The highest pTDS sample at 762 K may either be due to a partially released 1.9 eV trap or a filled 2.4 eV trap. The experimental TDS release temperature appears significantly higher than a 1.9 eV trap. By 762 K, an appreciable amount of vacancy agglomeration may have occurred during the peak-and-hold that is not modeled but may account for the higher temperature release. We also note that the results shown are based on the PTTP scheme that assumes a minimal separation in detrapping energies. For instance, a difference below 0.1 eV for consecutive detrapping energies leads to a significant error as outlined in [28]. Table 2 provides a summary of the resulting trap concentrations and energies found to give the best fit to the NRA and pTDS data with the least number of traps. The total trap concentration, $C^o(x)$, is shown in Fig. 7 (solid black) together with the kth trap concentration profiles, $C_k^o(x)$, given as the dot-dashed lines. The measured NRA profile from the "No pTDS" sample is also shown and has a shape that overlays with the $C^o(x)$ total trap concentration profile.

The simulated NRA profiles and final TDS release histories (dashed lines) are compared to the experimental data (solid lines) in Figs. 8 and 9 respectively. The simulated NRA and TDS produced reasonable fits with normalized fit metric values of ~0.7 for both. A possible reason for the discrepancy may be due to using detrapping energies separated by at least 0.1 eV. For instance, what appears as a single peak in Fig. 9 can be made of several nearby detrapping energies. If three detrapping energies made the peak near 620 K, the lowest energy may be completely released, the middle partially,
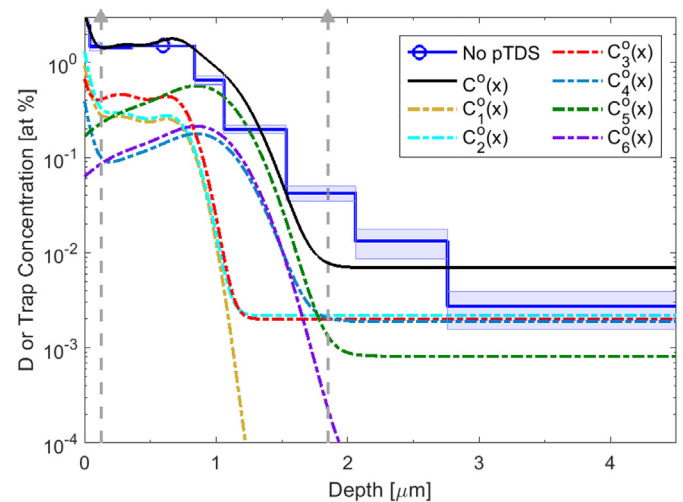
Table 2
Summary of the best fit parameters for each trap (k). The peak concentrations (C_k^j) in each zone (j) and the detrapping energies (E_k) modeled using the PTTP scheme. Reduced trap fraction ($\delta_k(T_{anneal}) = 1 - C_k(T_{anneal})/C_k(300)$) for each annealing temperature in Kelvin estimated from Ref. [38].

k	C_k^I	C_k^{II}	$f_k^{II}(x)$	C_k^{III}	E_k	$\delta_k(300)$	$\delta_k(573)$	$\delta_k(873)$
1	0.80	0.26	Empirical	0.0001	1.01	0	1	36
2	1.18	0.28	Empirical	0.0022	1.19	0	44	63
3	0.45	0.43	Empirical	0.0020	1.39	0	32	51
4	0.34	0.15	SRIM	0.0019	1.57	0	44	61
5	0.00	0.48	SRIM	0.0008	1.76	0	8	50
6	0.00	0.23	SRIM	0.0000	1.93	0	0	2
	[at.%]	[at.%]	Profile	[at.%]	[eV]	[%]	[%]	[%]

Fig. 7. The total trap concentration (black) compared to the "No pTDS" NRA data (blue). The individual trap concentrations for $k = 1-6$ are shown as dot-dashed lines. (For interpretation of the references to color in this figure legend, the reader is referred to the Web version of this article.)
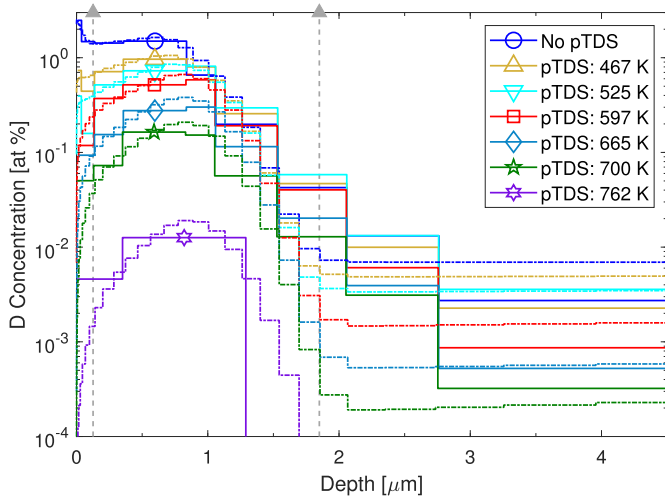
Fig. 8. The comparison of the NRA data (solid) and the simulation result (dashed) using the optimized fit parameters, summarized in Table 2. For clarity, only 4 samples are shown.

and the highest remained filled for a pTDS at 467 K (gold). As pointed out by Efimov et al. [13], several more intermediate pTDS peak-and-hold temperatures would be needed to discern if this was indeed the case.

5. Discussion

The detrapping energies found here are similar to values observed in previous studies as described in the Introduction. Some defects associated with the two lowest energies near 1.0 and 1.2 eV are likely grain boundaries and dislocations as seen in the control sample without heavy ion damage. In addition, the spatial segregation of defects observed for the lowest three detrap energies of 1.0, 1.2, and 1.4 eV are consistent with the multiple fill levels for mono-vacancies. The highest three detrap energies of 1.6, 1.8, and 1.9 eV are likely related to vacancy clusters. The various overlapping values do not contradict, but demonstrates that nearby detrapping energies are not fully resolved.

Recent work done with x-ray spectroscopy [40] has quantified the number of defects due to dislocation loops. For a single crystalline W sample damaged to 0.2 dpa with Cu ions at 5 MeV, the vacancy-type dislocation loop concentration was near 0.1 at.%. The scattering experiment was not spatially resolved but averaged over the first few microns of the W surface, and could not resolve

vacancy defects with radii below 5 Å. Thus that quoted vacancy concentration is for larger vacancy complexes averaged over the near-surface region and primarily includes large vacancy complexes. The x-ray scattering results indicated that the average size of a vacancy complex was (6.76±0.16) Å, which would correspond to a dislocation loop incorporating ∼30 W atoms. Traps 4–6 inferred in our work here have energies that are consistent with such larger vacancy complexes and have atomic concentrations of the same order of magnitude as these x-ray scattering results. Note that due to multiple occupancy, the concentration of D and traps are not likely one-to-one. The x-ray data also yields the size distribution, where the largest complexes are nearly two orders of magnitude lower in concentration than the smallest (5 Å) observable dislocation loop. Having the largest detrapping energy, the possible 7th is likely due to a large vacancy complex and has a concentration nearly two order of magnitude lower than traps 4–6. This initial necessarily brief comparison between our inferred results and the x-ray scattering results thus shows a similar order-of-magnitude defect density and similar inferred defect size. Clearly additional work focused on direct measurement of defects, determination of the corresponding trapping energies from computational modeling and D atom capacity is needed in order to determine if the observed D retention and release is self-consistent with actual defect structures produced in the W material.

The spatial segregation of ion damage-induced defects shown in Fig. 5 suggest insights into how to compare D retention from ion beam damage with what might be expected to occur from neutron damage. While the neutron only interacts with the nuclei of lattice W, the electronic stopping loss of heavy ions produces a distinctly unique profile for various defects. The significantly higher Primary Knock-on Atom (PKA) energy for heavy ions will create larger and denser collision cascades as well as overlapping sub-cascades [41]. Molecular dynamic modeling by Sand et al. [42] predicts no sub-cascade break-up below 150 keV. A threshold energy for break-up near 150 keV is predicted in Ref. [8] by comparing the similarity of D retention in neutron and heavy ion damaged W. Though the maximum heavy ion PKA energy (∼MeV) significantly exceeds the neutron PKA energy (∼300 keV), the threshold energy makes the sub-cascades comparable. Yet for heavy ions, the overlap of sub-cascades will increase and allow for more defect evolution (e.g. cluster formation) to occur as the cascades approach the Bragg peak. Our results show evidence for a significant deviation in the spatial location of high and low detrapping energies. The defects with higher detrapping energies (traps $k = 4–6$) correlate to the SRIM predicted Bragg peak while defects with low detrapping energies (e.g. mono-vacancies and small vacancy clusters) are located between the surface and the Bragg peak location. Noting that the
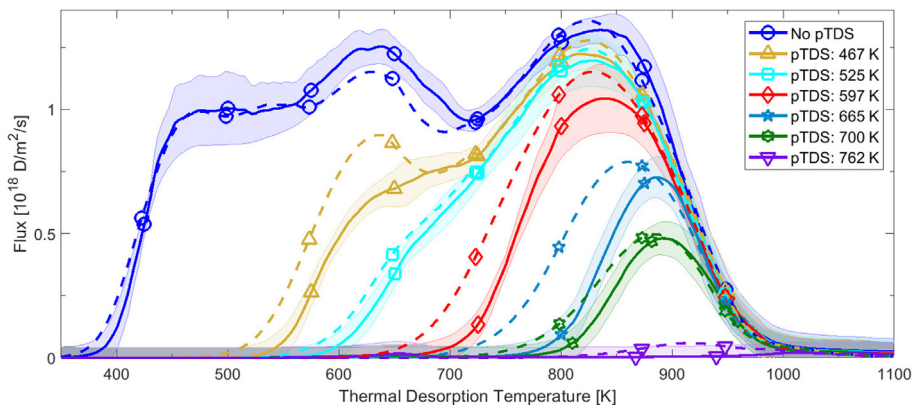

Fig. 9. The comparison of the TDS data (solid) and the simulation result (dashed) using the optimized fit parameters, summarized in Table 2.

neutron damage profile in PFMs should yield similar mono-vacancy and small vacancy clusters, we are then led to speculate that retention and release from such neutron-induced damage might appear similar to what we observe in the intermediate spatial region of our experiments.

Finally we note that SRIM is a kinetic Monte-Carlo code that does not simulate the accumulation or agglomeration of defects [43]. Each simulated energetic ion interacts with a new, undisturbed amorphous target that does not retain the induced damage from previous ions and thus has no memory. The formation of defect structures such as loops or clusters is not accounted for as only displacements are counted when collisions impart enough energy to a lattice atom (i.e. above the displacement threshold). Qualitatively, SRIM predicts that the density of collision cascades increases as the heavy ion projectile loses energy to recoils and the highest density occurs at the peak dpa depth. Closer to the surface, the initially highly energetic heavy ions impart less energy to lattice atoms and are more likely to form smaller collision cascades nearer to the surface. The result may then be a segregation of defects, with more lower-order vacancies produced towards the surface and larger vacancy clusters closer to the peak dpa zone.

6. Summary

Trapped D in Cu ion damaged W was sequentially depopulated with increasing temperature to determine the spatial profile and detrapping energies. The total D retention measured through pTDS, NRA, and TDS are shown to be in excellent agreement as well as demonstrating the repeatability of sample preparation. Comparing the NRA data from the control sample, without pTDS, and the lowest pTDS temperatures demonstrates that all of the plasma induced defects in the near-surface were depopulated by holding the sample at 597 K. In addition, the majority of retained D is depopulated by a pTDS temperature of 762 K. For pTDS peak-and-hold temperatures between 525 and 762 K, the D profiles measured via NRA are similar to the displacement damage profile predicted by SRIM. The full cycle of D_2 plasma loading, to pTDS, and finally a final TDS cycle was modeled with TMAP7 utilizing a Pseudo Trap and Temperature Partition (PTTP) scheme. Detrapping energies near 1.0, 1.2, 1.4, 1.6, 1.8, and 1.9 eV were found to fit the experimental data.

Appendix A. Supplementary data

Supplementary data to this article can be found online at https://doi.org/10.1016/j.jnucmat.2019.05.016.

Data availability

The raw/processed data required to reproduce these findings cannot be shared at this time as the data also forms part of an ongoing study. Data requests and inquiries may be sent to the primary author.

References

[1] V. Philipps, Tungsten as material for plasma-facing components in fusion devices, J. Nucl. Mater. 415 (2011) S2–S9. Proceedings of the 19th International Conference on Plasma-Surface Interactions in Controlled Fusion.

[2] A. E521, Standard Practice for Neutron Radiation Damage Simulation by Charged-Particle Irradiation, 1996. Reapproved 2009.

[3] O.V. Ogorodnikova, Fundamental aspects of deuterium retention in tungsten at high flux plasma exposure, J. Appl. Phys. 118 (2015), 074902.

[4] E.A. Hodille, A. Zalonik, S. Markelj, T. Schwarz-Selinger, C.S. Becquart, R. Bisson, C. Grisolia, Simulations of atomic deuterium exposure in self-damaged tungsten, Nucl. Fusion 57 (2017), 056002.

[5] W. Xiao, W. Geng, Role of grain boundary and dislocation loop in h blistering in w: a density functional theory assessment, J. Nucl. Mater. 430 (2012) 132–136.

[6] K. Heinola, T. Ahlgren, K. Nordlund, J. Keinonen, Hydrogen interaction with point defects in tungsten, Phys. Rev. B 82 (2010), 094102.

[7] N. Fernandez, Y. Ferro, D. Kato, Hydrogen diffusion and vacancies formation in tungsten: density functional theory calculations and statistical models, Acta Mater. 94 (2015) 307–318.

[8] O.V. Ogorodnikova, V. Gann, Simulation of neutron-induced damage in tungsten by irradiation with energetic self-ions, J. Nucl. Mater. 460 (2015) 60–71.

[9] V.K. Alimov, B. Tyburska-Pschel, Y. Hatano, J. Roth, K. Isobe, M. Matsuyama, T. Yamanishi, The effect of displacement damage on deuterium retention in iter-grade tungsten exposed to low-energy, high-flux pure and helium-seeded deuterium plasmas, J. Nucl. Mater. 420 (2012) 370–373.

[10] A. Debelle, M.F. Barthe, T. Sauvage, First temperature stage evolution of irradiation-induced defects in tungsten studied by positron annihilation spectroscopy, J. Nucl. Mater. 376 (2008) 216–221.

[11] S. Ryabtsev, Y. Gasparyan, M. Zibrov, A. Shubina, A. Pisarev, Deuterium thermal desorption from vacancy clusters in tungsten, Nucl. Instrum. Methods Phys. Res. Sect. B Beam Interact. Mater. Atoms 382 (2016) 101–104. The 21st International workshop on Inelastic Ion Surface Collisions (IISC-21).

[12] M.H.J. 't Hoen, M. Mayer, A.W. Kleyn, H. Schut, P.A.Z. van Emmichoven, Reduced deuterium retention in self-damaged tungsten exposed to high-flux plasmas at high surface temperatures, Nucl. Fusion 53 (2013), 043003.

[13] V.S. Efimov, Y.M. Gasparyan, A.A. Pisarev, Investigation of a fine structure of deuterium thermal desorption spectra from tungsten, J. Surface Invest. X-ray Sync. Neutron Techniques 7 (2013) 472–478.

[14] F. Ferroni, X. Yi, K. Arakawa, S.P. Fitzgerald, P.D. Edmondson, S.G. Roberts, High temperature annealing of ion irradiated tungsten, Acta Mater. 90 (2015) 380–393.

[15] M. Zhao, Q. Zhou, M. Nakata, A. Togari, F. Sun, Y. Hatano, N. Yoshida, Y. Oya, Deuterium removal efficiency in tungsten as a function of hydrogen ion beam fluence and temperature, in: G. Laukaitis (Ed.), Recent Advances in Technology Research and Education, Springer International Publishing, Cham, 2019, pp. 20–27.

[16] A. Zalonik, S. Markelj, T. Schwarz-Selinger, K. Schmid, Deuterium atom loading of self-damaged tungsten at different sample temperatures, J. Nucl. Mater. 496 (2017) 1–8.

[17] M.J. Simmonds, Y.Q. Wang, J.L. Barton, M.J. Baldwin, J.H. Yu, R.P. Doerner, G.R. Tynan, Reduced deuterium retention in simultaneously damaged and annealed tungsten, J. Nucl. Mater. 494 (2017) 67–71.

[18] T. Schwarz-Selinger, Deuterium retention in mev self-implanted tungsten: influence of damaging dose rate, Nuclear Mater. Energy 12 (2017) 683–688. Proceedings of the 22nd International Conference on Plasma Surface Interactions 2016, 22nd PSI.

[19] J.L. Barton, Y.Q. Wang, T. Dittmar, R.P. Doerner, G.R. Tynan, Deuterium retention in tungsten after heavy ion damage and hydrogen isotope exchange in {PISCES}, Nucl. Instrum. Methods Phys. Res. Sect. B Beam Interact. Mater. Atoms 332 (2014) 275–279.

[20] R.E. Stoller, M.B. Toloczko, G.S. Was, A.G. Certain, S. Dwaraknath, F.A. Garner, On the use of {SRIM} for computing radiation damage exposure, Nucl. Instrum. Methods Phys. Res. Sect. B Beam Interact. Mater. Atoms 310 (2013) 75–80.

[21] G.R. Tynan, A.D.B III, G.A. Campbell, R. Charatan, A. de Chambrier, G. Gibson, D.J. Hemker, K. Jones, A. Kuthi, C. Lee, T. Shoji, M. Wilcoxson, Characterization of an azimuthally symmetric helicon wave high density plasma source, J. Vacuum Sci. Technol. A 15 (1997) 2885–2892.

[22] K.J. Taylor, S. Yun, G.R. Tynan, Control of plasma parameters by using noble gas admixtures, J. Vacuum Sci. Technol. A: Vacuum, Surfaces, and Films 22 (2004) 2131–2138.

[23] M. Mayer, E. Gauthier, K. Sugiyama, U. von Toussaint, Quantitative depth profiling of deuterium up to very large depths, Nucl. Instrum. Methods Phys. Res. Sect. B Beam Interact. Mater. Atoms 267 (2009) 506–512.

[24] K. Schmid, U. von Toussaint, Statistically sound evaluation of trace element depth profiles by ion beam analysis, Nucl. Instrum. Methods Phys. Res. Sect. B Beam Interact. Mater. Atoms 281 (2012) 64–71.

[25] J.H. Yu, M.J. Simmonds, M.J. Baldwin, R.P. Doerner, Deuterium desorption from tungsten using laser heating, Nuclear Mater. Energy 12 (2017) 749–754. Elsevier.

[26] O.V. Ogorodnikova, J. Roth, M. Mayer, Deuterium retention in tungsten in dependence of the surface conditions, J. Nucl. Mater. 313–316 (2003)

469–477. Plasma-Surface Interactions in Controlled Fusion Devices 15.

[27] R. Bisson, S. Markelj, O. Mourey, F. Ghiorghiu, K. Achkasov, J.-M. Layet, P. Roubin, G. Cartry, C. Grisolia, T. Angot, Dynamic fuel retention in tokamak wall materials: an in situ laboratory study of deuterium release from polycrystalline tungsten at room temperature, J. Nucl. Mater. 467 (1) (2015) 432–438.

[28] M.J. Simmonds, J.H. Yu, Y.Q. Wang, M.J. Baldwin, R.P. Doerner, G.R. Tynan, Expanding the capability of reaction-diffusion codes using pseudo traps and temperature partitioning: applied to hydrogen uptake and release from tungsten, J. Nucl. Mater. 508 (2018) 472–480.

[29] O.V. Ogorodnikova, J. Roth, M. Mayer, Ion-driven deuterium retention in tungsten, J. Appl. Phys. 103 (2008) 034902.

[30] M. Poon, A.A. Haasz, J.W. Davis, Modeling deuterium release during thermal desorption of d+ -irradiated tungsten, J. Nucl. Mater. 374 (2008) 390–402.

[31] A. Rusinov, Y. Gasparyan, N. Trifonov, A. Pisarev, S. Lindig, M. Sakamoto, Investigation of hydrogen-defect interaction in tungsten by the probe fluence method, J. Nucl. Mater. 415 (2011) S645–S648. Proceedings of the 19th International Conference on Plasma-Surface Interactions in Controlled Fusion.

[32] B. Merrill, J. Jones, D. Holland, Tmap/mod 1: Tritium Migration Analysis Program Code Description and User's Manual, Idaho National Engineering Laboratory EGG-EP-7407, EG and G, 1986.

[33] G. Longhurst, Tmap7 User Manual, Idaho National Engineering and Environment Laboratory INEEL/EXT-04-02352(Rev. 2), 2008.

[34] J. Ambrosek, G.R. Longhurst, Verification and Validation of Tmap7, Idaho National Engineering and Environment Laboratory INEEL/EXT-04-01657 (Rev. 2), 2008.

[35] M.A. Pick, K. Sonnenberg, A model for atomic hydrogen-metal interactions application to recycling, recombination and permeation, J. Nucl. Mater. 131 (1985) 208–220.

[36] W. Eckstein, Calculated sputtering, reflection and range values, IPP-Report IPP 9/132 (2002).

[37] L. Gao, W. Jacob, U. von Toussaint, A. Manhard, M. Balden, K. Schmid, T. Schwarz-Selinger, Deuterium supersaturation in low-energy plasma-loaded tungsten surfaces, Nucl. Fusion 57 (2017), 016026.

[38] S. Sakurada, K. Yuyama, Y. Uemura, H. Fujita, C. Hu, T. Toyama, N. Yoshida, T. Hinoki, S. Kondo, M. Shimada, D. Buchenauer, T. Chikada, Y. Oya, Annealing effects on deuterium retention behavior in damaged tungsten, Nuclear Mater. Energy 9 (2016) 141–144.

[39] S. Kirkpatrick, C.D. Gelatt, M.P. Vecchi, Optimization by simulated annealing, Science 220 (1983) 671–680.

[40] P. Sun, Y. Wang, M. Frost, C. Schnwlder, A.L. Levitan, M. Mo, Z. Chen, J.B. Hastings, G.R. Tynan, S.H. Glenzer, P. Heimann, Characterization of defect clusters in ion-irradiated tungsten by x-ray diffuse scattering, J. Nucl. Mater. 510 (2018) 322–330.

[41] P. Vladimirov, S. Bouffard, Displacement damage and transmutations in metals under neutron and proton irradiation, Compt. Rendus Phys. 9 (2008) 303–322 (Materials subjected to fast neutron irradiation).

[42] A.E. Sand, S.L. Dudarev, K. Nordlund, High-energy collision cascades in tungsten: dislocation loops structure and clustering scaling laws, EPL (Europhysics Letters) 103 (2013) 46003.

[43] J. Ziegler, J. Biersack, U. Littmark, The Stopping and Range of Ions in Matter, Pergamon Press, 1985.